Aerospace Science and Technology, Volume 91, August 2019, pp. 287-300
DOI: 10.1016/j.ast.2019.05.034

Unsteady Detached-Eddy Simulation (DES) of the Jetstream 31 Aircraft in One Engine Inoperative (OEI) Condition with Propeller Modelling

Loris Casadei[a], László Könözsy[a,*], Nicholas J. Lawson[b]

[a] *Centre for Computational Engineering Sciences, Cranfield University, Cranfield, Bedfordshire, MK43 0AL, United Kingdom*
[b] *National Flying Laboratory Centre, Cranfield University, Cranfield, Bedfordshire, MK43 0AL, United Kingdom*

Abstract

Numerical results from a three-dimensional (3D) computational fluid dynamics (CFD) model of the Jetstream 31 aircraft in conditions of one engine inoperative are presented. The objective of this work is to analyse the performance of the Jetstream 31 aircraft and provide transient data using an unsteady Detached-Eddy Simulation (DES) CFD approach and a numerical propeller model to compare computational results with a single engine flight test experiment. The propeller modelling approach has been implemented through User-Defined Functions using C programming language to replicate the propeller effect. Different angles of attack and sideslip are studied, based on records from flight test data, both with unsteady (DES) and steady-state Reynolds-Averaged Navier-Stokes (RANS) models. An error analysis on the flight test data provides an error band from 2% to 16% among all cases, high values due to the lack of many data samples. Across the RANS approach, an average deviation of 6.9% and 3.8% for respectively lift and drag coefficients is achieved. By applying the DES turbulence modelling approach, a better lift prediction is achieved (5.4%) despite a slightly worse drag (4.5%). It has also been found that 80% of the numerical results are within the error band defined. A close agreement has been found within moment coefficients, with average percentage deviations from 3.3% to 7.0%. Overall, an analysis has been carried out in the present work, both on the flight test and computational sides to provide reliable numerical results of these aerodynamic properties.

Keywords: Unsteady Turbulent Flows, Detached-Eddy Simulation (DES), Unsteady Aerodynamics, Full Aircraft Simulation, Drag and Lift Prediction, Pressure Coefficients, Moment Coefficients, Experimental Flight Test

---

1. Introduction

In the last five decades, the advances in computer engineering have allowed application of Computational Fluid Dynamics (CFD) in many industrial design departments and research fields. One of these is the aerospace sector, which mainly adopts this tool for aircraft aerodynamics and performance estimation.

---

[*] Corresponding author
Email address: `laszlo.konozsy@cranfield.ac.uk` (László Könözsy)

Preprint submitted to Aerospace Science and Technology *11th May 2019*

First studies with CFD on simple inviscid two-dimensional problems originates from the 1970s. In the 1980s the interest started to be focus on viscous problems and turbulence models began to be developed [1]. Only from the 1990s, reliable results of three-dimensional flow problems had the computational requirements to be performed [2]. It has been recognized in Johnson's work (2003) [3], how in these latter 30 years, CFD started to assume a more relevant role in the development of new generation aircrafts. For example, CFD investigations for aerospace applications were extensively carried out recently by Ekaterinaris (2004) [4], Kyrkos and Ekaterinaris (2012) [5], Kontogiannis and Ekaterinaris (2013) [6], Gómez et al. (2014) [7], Ghoreyshi et al. (2016) [8], Kontogiannis et al. (2016) [9], Nelson et al. (2017) [10], Lawson et al. (2017) [11], Misaka and Obayashi (2017) [12], and Righi et al. (2018) [13].

Considering different simulation techniques, the Direct Numerical Simulation (DNS) is the closest attempt up-to-date to overcome the CFD limitations, its only error being in the numerical discretization scheme. However, its applications are still limited to relatively simple benchmark problems, because the amount of calculations required is depending on the flow Reynolds number with the power $Re^{9/4}$ [14, 15]. It therefore becomes clear, when aerospace problems are faced, that DNS cannot easily be considered as the method to use, as typical Reynolds numbers of aerospace flows are of the order of 10^6 and 10^7. The Large-Eddy Simulation (LES) technique is a currently wide-spread model, introduced by Smagorinsky (1963) [16], which requires fewer resources: $Re^{0.4}$ for the outer layer and $Re^{1.8}$ for the viscous sublayer, where in aeronautics there is approximately 1% of the boundary layer thickness [17]. However it is still high for aerospace solutions, as Spalart et al. [18] estimated 10^{11} grid points and 5×10^6 time steps would be required with mathematical and engineering assumptions to provide a reliable numerical solution. The most immediate choice for a rapid and reliable solution falls then in the Reynolds-Averaged Navier-Stokes (RANS) equations, where transport equation turbulence models allow a consistent formulation for every grid and geometry independently from their complexity [19]. Therefore, the steady-state RANS and its time-dependent version, unsteady RANS (URANS), are well-established approaches for aerospace and other industrial applications.

The Detached-Eddy Simulation (DES) technique was frequently used recently for aerospace applications offering a compromise between LES and RANS, a less expensive unsteady model of acceptable computational requirements. The concept of the DES modelling approach was introduced by Spalart et al. (1997) [18] to accelerate the use of subgrid-scale models in aerospace industry and firstly applied on a three-dimensional wing in 1999 [20]. The DES approach employs an LES treatment in the separated regions and unsteady RANS (URANS) in the boundary layer. Therefore, large-scale unsteady turbulence, which plays a dominant role in the outer layer, is better captured by exact resolution, while the usage of URANS instead of SGS models of LES-type in the subgrid layer, reduces the computational cost and the necessity of a refined mesh. Its motivation has remained unvaried throughout the years: to model high-Reynolds number and highly separated flows, which are common conditions in aerospace applications and studies [21]. Its advantages are significant, as shown in the first analysis carried out by Shur et al. [20], where lift and drag are predicted within 10% from the experimental results at all angles of attack up to 90 degrees. Since, unsteady flow problems are in the centre of research interest for aerospace applications, see, e.g., in the works of Jacquin et al. [22], Huang and Ekici [23], Ghoreyshi et al. [24], and Ghoreyshi and Cummings [25], therefore, the concept of the DES approach offers a potential possibility to investigate unsteady flow around an aircraft. Further CFD investigations in conjunction with the DES technique were carried out recently by Bunge et al. (2007) [26], Lawson and Barakos (2010) [27], Sun et al. (2013) [28], Cummings and Schütte (2013) [29], Mirzaei and Sohankar (2015) [30], Šekutkovski et al. (2016) [31], Nicolás-Pérez et al. (2017) [32], and Zhou et al. (2018) [33].

Figure 1: Jetstream 31 aircraft owned by Cranfield University, United Kingdom [34]

Aircraft simulations and flight testing are playing a key role to support our understanding of flight physics and aerodynamics [11, 35–40]. Therefore, several experimental and computational aerodynamics studies on the Jetstream 31 aircraft (see Figure 1) have been carried out in the National Flying Laboratory Centre (NFLC) at Cranfield University in the last decade. This has been possible by comparing CFD simulations with real flight test data taken from the NFLC-A Jetstream aircraft owned by the university. However, no transient data were available on this aircraft, therefore, the objective of the present work is to analyse the performance of a Jetstream 31 aircraft in a One-Engine-Inoperative (OEI) condition, making use of an unsteady DES CFD simulation approach and a numerical propeller model to compare computational results with a single engine flight test experiment.

An important advantage of CFD is its capability in simulating extreme scenarios, which are impossible or unable to be reproduced in a laboratory or wind tunnel [41]. An example is the evaluation of safety measures and accident studies such as the OEI condition in aircraft development. Flight testing remains the best representation of flight physics and it is not fully replaceable by any other methodology, at the time of writing. However, with DES it may be possible to simulate any flight condition, allowing a detailed analysis of the aerodynamics. OEI conditions can happen in multi-engine aircraft in case of malfunction or power loss of one or more engines, resulting in an asymmetric flight condition if the engine is not mounted on the vehicle centerline. Multi-engine airplanes are built in a way in which they can safely operate even in case of an engine failure. Therefore, detailed understanding of the aircraft aerodynamics under these OEI conditions offers a potential safety benefit through improvements in aircraft performance.

2. Governing Equations

2.1. Detached-Eddy Simulation (DES) turbulence modelling approach

The Detached-Eddy Simulation (DES) is a form of a hybrid LES/RANS turbulence modelling approach which employs a Large-Eddy Simulation (LES) treatment in the separated regions and an unsteady RANS (URANS) approach in the boundary layer [18, 20]. In the present study, within the framework of the DES turbulence modelling concept, the *Realizable* $k-\varepsilon$ model has been used for the URANS modelling approach. All simulations have been performed with the use of the ANSYS-FLUENT commercial software package in accordance with the turbulence dependency study carried out in [42]. The dissipation term of the URANS approach is predicted by

$$D_k = \frac{\rho k^{\frac{3}{2}}}{l_{des}}, \tag{1}$$

where the characteristic length scale of the DES approach is defined by

$$l_{des} = min(l_{rke}, l_{les}), \tag{2}$$

which is the minimum of the length scales of the *Realizable* $k-\varepsilon$ model and the LES approach, where

$$l_{rke} = \frac{k^{\frac{3}{2}}}{\varepsilon}, \tag{3}$$

and

$$l_{les} = C_{des}\Delta_{max}, \tag{4}$$

where k is turbulent kinetic energy, ε is the turbulent kinetic energy dissipation, $C_{des} = 0.61$ is a constant of the DES approach, and Δ_{max} is the maximum grid spacing. The improved *Delayed DES* (DDES) approach is adopted in the present work, where the length scale l_{ddes} of the DDES model is predicted by

$$l_{ddes} = l_{rke} - f_d \max(0, l_{rke} - C_{des}\Delta_{max}), \tag{5}$$

where the distance function f_d is defined by

$$f_d = 1 - \tanh\left[(20r_d)^3\right] \tag{6}$$

with the parameter r_d which can be given by

$$r_d = \frac{\nu_t + \nu}{\sqrt{U_{i,j}U_{i,j}}\kappa^2 d^2}, \tag{7}$$

where ν_t is the kinematic eddy viscosity, ν is the kinematic viscosity, $U_{i,j}U_{i,j}$ is the double dot scalar product of the mean velocity gradient tensor, $\kappa = 0.41$ is the von Kármán constant, and d is the distance to the closest wall. In regards to the filtered regions, the LES viscous model has been employed, which adopts the Boussinesq hypothesis to relate Reynolds stress tensor and the mean rate-of-strain given by

$$-\rho\overline{u_i'u_j'} = \mu_t\left(\frac{\partial u_i}{\partial x_j} + \frac{\partial u_j}{\partial x_i}\right) - \frac{2}{3}\left(\rho k + \mu_t\frac{\partial u_k}{\partial x_k}\right)\delta_{ij}, \tag{8}$$

where ρ is the density of the fluid, u_i' is the fluctuating velocity vector, μ_t is the dynamic eddy viscosity, and δ_{ij} represents the unit tensor using Cartesian index notation. The advantage of this assumption is the relatively low computational cost correlated to the calculation of the dynamic eddy viscosity μ_t. However, the drawback is the assumption of μ_t as an isotropic scalar quantity, not strictly true. For compressible turbulent flows, the subgrid-scale turbulent stresses can be computed in the Favre-Filtered Navier-Stokes equations by

$$\tau_{ij} = \overline{\rho}\widetilde{u_iu_j} - \overline{\rho}\tilde{u}_i\tilde{u}_j, \tag{9}$$

where the left hand side can be decomposed into deviatoric and isotropic parts as

$$\tau_{ij} = \underbrace{\tau_{ij} - \frac{1}{3}\tau_{kk}\delta_{ij}}_{\text{deviatoric}} + \underbrace{\frac{1}{3}\tau_{kk}\delta_{ij}}_{\text{isotropic}}, \tag{10}$$

where τ_{kk} represents the diagonal elements of the subgrid-scale stress tensor in the isotropic part, which is not modelled. The deviatoric part can be modelled with the compressible form of the Smagorinsky model [16] as

$$\tau_{ij} - \frac{1}{3}\tau_{kk}\delta_{ij} = -2\mu_t(S_{ij} - \frac{1}{3}S_{kk}\delta_{ij}), \tag{11}$$

where μ_t denotes the subgrid-scale turbulent viscosity which is modelled by the Smagorinsky-Lilly approach as

$$\mu_t = \rho L_s^2 |\overline{S}|, \tag{12}$$

where the subgrid-scale mixing length can be defined by

$$L_s = min(\kappa d, C_s \Delta), \tag{13}$$

where d denotes again the distance to the closest wall, C_s is the Smagorinsky constant, Δ is the local grid size, and the magnitude of the rate-of-strain (deformation) tensor for the resolved scale $|\overline{S}|$ can be computed as

$$|\overline{S}| \cong \sqrt{2\overline{S}_{ij}\overline{S}_{ij}}. \tag{14}$$

The choice of the C_s constant revealed to be problematic and dependant on the flow case. Germano et al. [43] and Lilly [44] designed a procedure to dynamically evaluate C_s based on the solution already computed, making the user free from having to choose its value. This methodology is known as the *Dynamic Smagorinsky-Lilly* model (DSLM) to evaluate the subgrid-scale turbulent viscosity. It consists in applying a second filter $\hat{\Delta}$ which is equal to twice Δ and evaluate two different filtered relations for the subgrid-scale stress tensor given by

$$\tau_{ij} = -2C\overline{\rho}\Delta^2|\tilde{S}|\left(\tilde{S}_{ij} - \frac{1}{3}\tilde{S}_{kk}\delta_{ij}\right), \tag{15}$$

$$T_{ij} = -2C\widehat{\overline{\rho}}\hat{\Delta}^2|\hat{\tilde{S}}|\left(\hat{\tilde{S}}_{ij} - \frac{1}{3}\hat{\tilde{S}}_{ij} - \frac{1}{3}\hat{\tilde{S}}_{kk}\delta_{ij}\right). \tag{16}$$

where the coefficient C is assumed to be independent by the filtering process and defined by

$$C = C_s^2 \qquad ; \qquad C_s = \sqrt{C}. \tag{17}$$

The Germano proposed an identity in [43] which relates the two filtered subgrid-scale stresses as

$$L_{ij} = T_{ij} - \hat{\tau}_{ij} = \overline{\rho}\widehat{\tilde{u}_i\tilde{u}_j} - \frac{1}{\overline{\hat{\rho}}}(\widehat{\overline{\rho}\tilde{u}_i}\,\widehat{\overline{\rho}\tilde{u}_j}), \tag{18}$$

where L_{ij} is the resolved turbulent stress tensor for the large eddy field and the coefficient C can be expressed [44] by

$$C = \frac{(L_{ij} - L_{kk}\delta_{ij}/3)M_{ij}}{M_{ij}M_{ij}}, \tag{19}$$

where M_{ij} is the anisotropic part of T_{ij} defined by

$$M_{ij} = -2(\hat{\Delta}^2\hat{\overline{\rho}}|\hat{\tilde{S}}|\hat{\tilde{S}}_{ij} - \Delta^2\overline{\rho}\widehat{|\tilde{S}|\tilde{S}_{ij}}). \tag{20}$$

2.2. Propeller theory and CFD modelling

Initial CFD modelling of the Jetstream 31 aircraft using RANS turbulence models was presented by [45] and [42]. Propeller flows are still challenging tasks for CFD, because of the high unsteadiness and complex flow phenomena around propellers are two of main reasons for the difficulties related to modelling this kind of flow [46]. The propeller influences the flow downstream perceived by the wing. The swirling motion gives to the fluid flow an increase in axial velocity and a pressure jump. As suggested by Westmoreland [47], two methods can be adopted:

- real propeller model with blades and rotating mesh;
- actuator disk of zero thickness with jump condition.

The first method is potentially more accurate giving more realistic flow conditions. However, the actuator disk method is able to give reliable results with a sensitively reduced computational power, as shown by Phillips [48] and Zondervan [49]. Using this method, we can now define the velocity and pressure jumps. In the present study, this is done through a User-Defined Function (UDF) implementation of the General Momentum Theory (GMT), based on the work of Lino [50]. The equations involved are thoroughly discussed in [45] and [42], to which we refer for deriving the UDF model of this work. There are a number of limitations of this method: the upwash effect from the wing is not taken into account and the theory is based on an inviscid and incompressible model, where no unsteady effects are considered. As a result, the jump condition can be defined for the pressure and the tangential velocity as

$$\Delta p = A_1 r_p^2 + B_1, \tag{21}$$

$$V_t = C_1 r_p, \tag{22}$$

where parameters A_1, B_1 and C_1 are computed as

$$\begin{cases} A_1 = \rho\omega_s^2\left(1 - \dfrac{V_\infty + V_i}{2V_{xs}}\right)\dfrac{V_\infty + V_i}{V_{xs}}, \\ B_1 = \dfrac{\rho}{2}(V_{xs}^2 - V_\infty^2) - \rho\omega_s^2\dfrac{V_\infty + V_i}{V_x s}r_p^2, \\ C_1 = \dfrac{V_\infty + V_i}{V_x s}\omega_s, \end{cases} \tag{23}$$

where $\omega_s = 4V_i \frac{V_\infty + 2V_i}{\Omega r_p^2}$ and $V_{xs} = V_\infty + 2V_i$, and the induced velocity V_i can be given by

$$V_i = \sqrt{\frac{V_\infty^2}{4} + \Omega^2 r_p^2 \left(1 - \sqrt{1 - \frac{4T}{A_p \rho \Omega^2 r_p^2}}\right)} - \frac{V_\infty}{2}, \tag{24}$$

which is the function of the propeller rotational speed Ω, surface area of the propeller A_p, propeller radius r_p, thrust T and the free-stream velocity V_∞. The three coefficients A_1, B_1 and C_1 have been calculated with an Excel macro for each case and these equations have been implemented in a C programming language based User-Defined Function (UDF) using the ANSYS-FLUENT software package environment. The input variables required for the macro are: a) number of blades, b) blade radius, c) blade radius at the trailing edge, d) rotational speed of the propeller, e) propeller thrust, and f) free-stream conditions (static pressure, velocity). The propeller thrust is estimated using analysis of left and right engine parameters and True Air Speed (TAS) as outlined by Lawson et al. [11].

3. Methodology

3.1. Flight test validation

In the National Flying Laboratory Centre (NFLC) at Cranfield University, flight tests have been performed on the Jetstream 31 aircraft, a 19-seat twin-turboprop commuter airliner developed by British Aerospace in 1982. The semi-monocoque fail safe fuselage and fail safe wing structure are made of aluminium alloy construction and the cabin can be customised for different uses, from passenger carrier to air ambulance. The two engines are Honeywell TPE331 mounting Dowty 106 in (2.69 m) reversing four-bladed metal propellers. The technical specifications of the Jetstream 31 aircraft is summarised in Table 1.

Capacity	19+2 passengers	Max. speed	488 km/h
Length	14.37 m	Cruise speed	426 km/h
Wingspan	15.85 m	Stall speed	159 km/h
Height	5.32 m	Range	1260 km
Wing area	25.2 m^2	Service ceiling	7620 m
Airfoil	NACA 63A418 at root	Rate of climb	10.6 m/s
	NACA 63A412 at tip	Wing loading	276 kg/m^2
Empty weigth	4360 kg	Powerplant	701 kW each engine
Max. takeoff weigth	6950 kg	Power/mass	0.201 kW/kg

Table 1: Jetstream 31 technical specifications [51]

Single engine flight tests were also successfully performed in the NFLC at Cranfield University on the Jetstream 31 aircraft with a straight and level cruise condition. Different set of recordings have been done for both right or left engine shut down at different angles of attack and indicated air speeds. The parameters analysed in each test are

Thrust (T), Fuel mass (W_f), Equivalent Air Speed (EAS), Air temperature (AT), Altitude (H), Wing angle of attack at the root (α), Sideslip angle (β), Pitch angle (θ), Elevator, aileron and rudder deflection (η, ξ, ζ). Given the altitude H and the air temperature AT, the ambient pressure is evaluated with International Standard Atmosphere (ISA) by

$$p_\infty = p(1 - 6.8756 \times 10^{-6} H)^{5.2559}, \tag{25}$$

where p is the atmospheric pressure and the reference density with the perfect gas law can be expressed by

$$\rho_\infty = \frac{p_\infty}{RT_\infty}, \tag{26}$$

where R is the universal gas constant and T_∞ is the reference temperature. The aerodynamic forces drag and lift are indirectly evaluated, thus the lift force (L) is equated to the aircraft weight (W) and drag force (D) to the engine thrust with the following relationships

$$L = W - T\sin(\theta), \tag{27}$$

$$D = T\cos(\theta). \tag{28}$$

The lift and drag coefficients are defined based on the wing area of the aircraft and calculated by

$$C_L = \frac{2L}{\rho_\infty S_W V_\infty^2}, \tag{29}$$

$$C_D = \frac{2D}{\rho_\infty S_W V_\infty^2}, \tag{30}$$

where S_W is the wing surface area. The total mass of the aircraft, equated to lift is known, given the Zero-Fuel Mass (ZFM) of the aircraft, fuel and passenger masses. From previous work by Lawson et al. [11], the error band ranges in measuring mass, density, speed and angle of attack are presented in Table 2.

Variable	Standard Error
Aircraft empty mass	±0.1%
Passenger mass	±0.7%
Fuel mass	±0.3%
ADC air density ρ (kg/m^3)	±0.8%
True Air Speed TAS	±2 knots (±1.8% at 220 knots)
Angle of attack $\alpha(^\circ)$	±0.085°

Table 2: Estimated errors in mass and flight measurement [11]

Furthermore, with the known mass of the aircraft and through previous validation of the propeller thrust measurement [11], the errors in lift and drag coefficients from the flight test data are estimated (see Table 3).

Variable	Standard Error
C_D	±2.7%
C_L	±2.4%

Table 3: Estimated errors in aerodynamics coefficient measurement [11]

3.2. Computational mesh sensitivity investigations

The ICEM-CFD software package has been used to generate an unstructured hybrid mesh. Structured meshes were considered, but were not possible in the timeframe of the project and would not be expected to offer significant increases in accuracy in this case. Attention needs to be taken when choosing the prism layer thickness and first element height [34, 52, 53]. To evaluate the boundary layer thickness, the Reynolds number needs to be calculated by

$$Re = \frac{\rho_\infty V_\infty \bar{c}}{\mu_\infty}, \tag{31}$$

where $\bar{c}$ is the mean aerodynamic chord, and the dynamic viscosity μ_∞ is computed based on the Sutherland law as

$$\mu_\infty = \mu_0 \left(\frac{T_s}{T_0}\right)^{\frac{3}{2}} \frac{T_0 + T_{eff}}{T_s + T_{eff}}, \tag{32}$$

where μ_0 is the reference dynamic viscosity, T_s is the static temperature, T_0 is the reference temperature, and T_{eff} is an effective temperature (Sutherland constant). The boundary layer thickness can then be estimated with the formula for a turbulent zero pressure gradient flat plate as

$$\delta(x) = \frac{0.37x}{\sqrt[5]{Re}}. \tag{33}$$

Different velocities are going to be studied in this work, so the most extreme cases (highest speeds) are considered in order to determine a grid suitable for all the studies. A second important consideration needs to be taken for the first cell height. The dimensionless wall distance (or y^+) is a parameter describing how coarse or fine the mesh is for a particular flow pattern. A y^+ value of 1 indicates the grid is fine enough to capture the whole flow physics, while bigger values indicate the mesh is coarser than what required for an optimal resolution. In this study, a y^+ value of approximately 40 has been set as maximum limit, as a good compromise between computational resources available and expected accuracy. When extruding the prism layer, the growth ratio and number of layers have been chosen in order to have a total layer thickness equal to approximately 20% of the boundary layer thickness, equivalent to around

y^+ 1000 which guarantees adequate resolution of the log law region of the boundary layer, up to the outer layer.

Case	V_{max} (m/s)	Re $(\times 10^6)$	$20\%\,\delta(x)$ (mm)	First cell (mm)
Right Engine Off	94.597	8.07	5.28	0.2362
Left Engine Off	93.032	7.92	5.30	0.2404

Table 4: Boundary layer thickness details

The resulting mesh is shown in Figures 2 and 3. The black outline around the aircraft in Figure 2 represents the prism layer extrusion, much finer than the outer mesh. The chosen growth ratio also allowed to have a reasonable coarsening of the mesh while going towards the external boundaries, while the surface mesh is mostly uniform except in corners and discontinuities, where a refinement takes place. In Figure 3 a detail of the wing mesh is shown, where the mesh refinement can be seen near the tip and trailing edge.

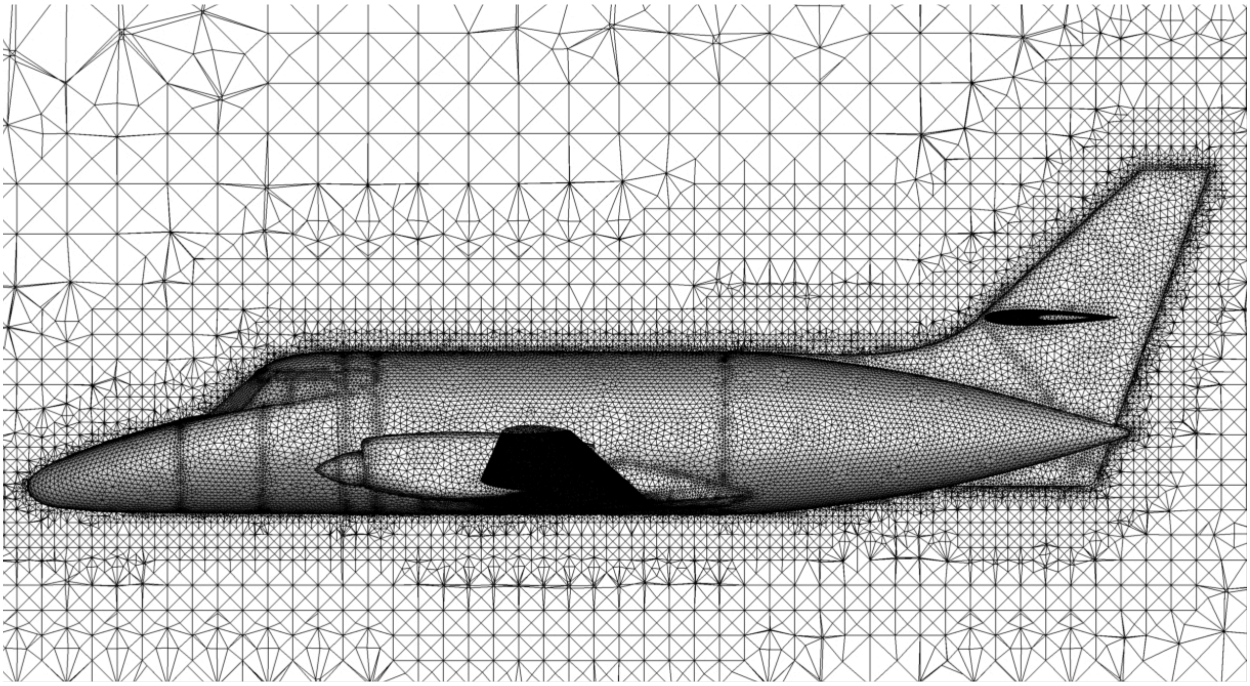

Figure 2: The generated computational mesh: symmetry plane XZ

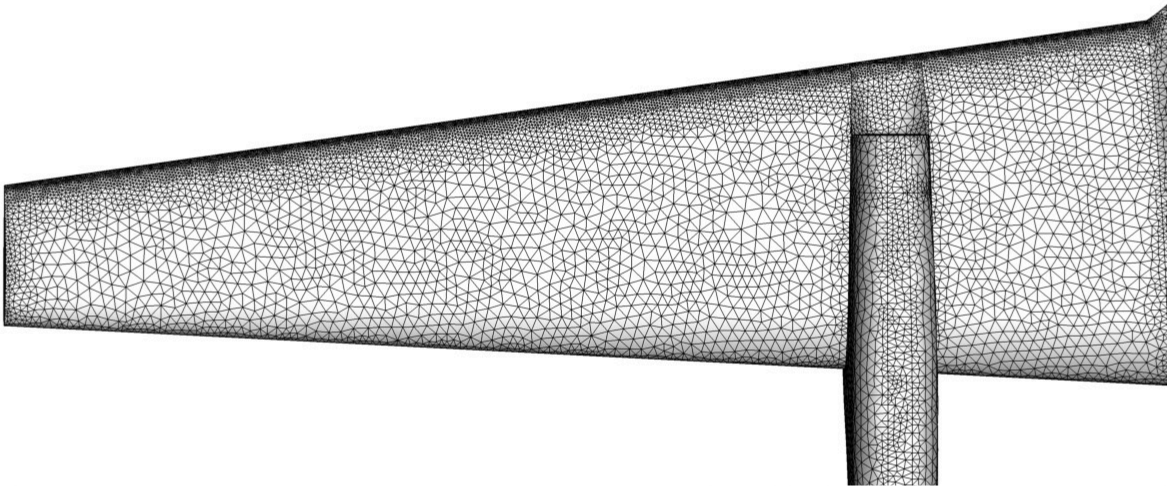

Figure 3: The generated computational mesh: wing details

3.3. Mesh verification

A grid convergence study was performed by Jacques [42] using the Spalart-Allmaras turbulence model, where 4 grids with further level of refinement were created. The verification and validation process proposed by Roache [54] for Computational Fluid Dynamics problems is adopted here as further confirmation of the grid convergence study previously carried out. The lowest and highest angles of attack cases have been computed with all grids, giving drag and lift coefficients as shown in Tables 5 and 6.

Mesh	Elements	C_L	$\Delta_{rel}(\%)$	C_D	$\Delta_{rel}(\%)$
Coarse	$3.0 \cdot 10^6$	0.4619	-	0.04361	-
Intermediate	$4.6 \cdot 10^6$	0.4632	0.27	0.04072	-6.64
Medium	$5.4 \cdot 10^6$	0.4640	0.17	0.04144	1.78
Fine	$7.4 \cdot 10^6$	0.4651	0.24	0.04041	-2.49

Table 5: Grid convergence study: low angle of attack [42]

Mesh	Elements	C_L	$\Delta_{rel}(\%)$	C_D	$\Delta_{rel}(\%)$
Coarse	$3.0 \cdot 10^6$	1.129	-	0.1670	-
Intermediate	$4.6 \cdot 10^6$	1.105	-2.20	0.1606	-3.84
Medium	$5.4 \cdot 10^6$	1.050	-4.95	0.1593	-0.80
Fine	$7.4 \cdot 10^6$	1.042	-0.72	0.1589	-0.25

Table 6: Grid convergence study: high angle of attack [42]

The Grid Convergence Index (GCI) has been used to provide a consistent manner in reporting results from grid convergence studies, as it provides an error band on the grid convergence of the solution [54]. The expected outcome is a numerical result reaching the exact solution when the grid resolution approaches zero. However, different factors might bring the numerical solution to converge to an asymptotic value different from the real solution.

The GCI is an index describing how far the computed result is from the asymptotic value, defining an error band and foreseeing how a further refinement would impact the solution. The solution on the grid level f_i is taken into account for grid convergence (drag and lift coefficient in this study), with f_3 related to the finer mesh and f_1 to the coarser, and f_2 to the medium. At this point, an approximation was required, due to the difficulty of maintaining a constant grid refinement ratio throughout consecutive refinements in unstructured meshes automatically generated. Specifically, the grid refinement ratio (γ) medium-intermediate is 1.17 and the fine-medium 1.38, so an intermediate value of 1.27 has been used for next calculations. The GCI is obtained by

$$GCI_{fine} = \frac{F_s|\Delta_{rel}|}{\gamma^n - 1}, \qquad GCI_{coarse} = \frac{F_s|\Delta_{rel}|\gamma^n}{\gamma^n - 1}, \tag{34}$$

where γ is the grid refinement ratio, F_s is a safety factor of 1.25 when three grids are considered and Δ_{rel} the relative deviation (error) calculated by

$$\Delta_{rel} = \frac{f_2 - f_1}{f_1}. \tag{35}$$

Finally, the asymptotic range of convergence R_a can be checked with the following equation, which should give approximately 1 with asymptotic behaviour given by

$$R_a = \frac{GCI_{fine}}{GCI_{coarse}\,\gamma^n}. \tag{36}$$

The lift coefficients from low angle of attack case have been taken as example to evaluate GCI indexes and asymptotic range (see Table 7).

GCI_{coarse} (%)	GCI_{fine} (%)	n	R_a
0.5757	0.7902	1.33	0.9983

Table 7: The Grid Convergence Index (GCI) for C_L at low angle of attack case

The time step size has been calculated based on the convection time as

$$t_{conv} = V_{TAS}\, l_a \tag{37}$$

where V_{TAS} the true air speed of each case and l_a is the aircraft length. The time step size has been taken as 1/25 of t_{conv} and the total simulation time as 30 t_{conv}, with 10 iterations per time step. A smaller time-step size equal to 1/50 of t_{conv} has also been considered to determine its effect on the solution. A single case study (Right engine off, highest speed and lowest angle of attack) has been taken as example for this comparisons and results (see Table 8).

Time step size	C_L Test	C_D Test	C_L	$\Delta_{rel}(\%)$	C_D	$\Delta_{rel}(\%)$
$t_{conv}/50$	0.5285	0.0450	0.5288	5.2	0.0428	1.2
$t_{conv}/25$	0.5285	0.0450	0.5291	5.2	0.0427	0.9

Table 8: Grid and time step size dependence study

According to our numerical experiments, the finer time step size did not give significant improvements, thus allowing the smaller step size to be used for all DES simulations in this study.

3.4. Boundary conditions and computational setup

The outer domain consists of a cylinder with upstream and downstream surfaces placed at 10 fuselage lengths and a radius of 5 fuselage lengths [55]. These dimensions are sufficiently large to ensure pressure far field boundary conditions. The resulting domain is shown in Figure 4.

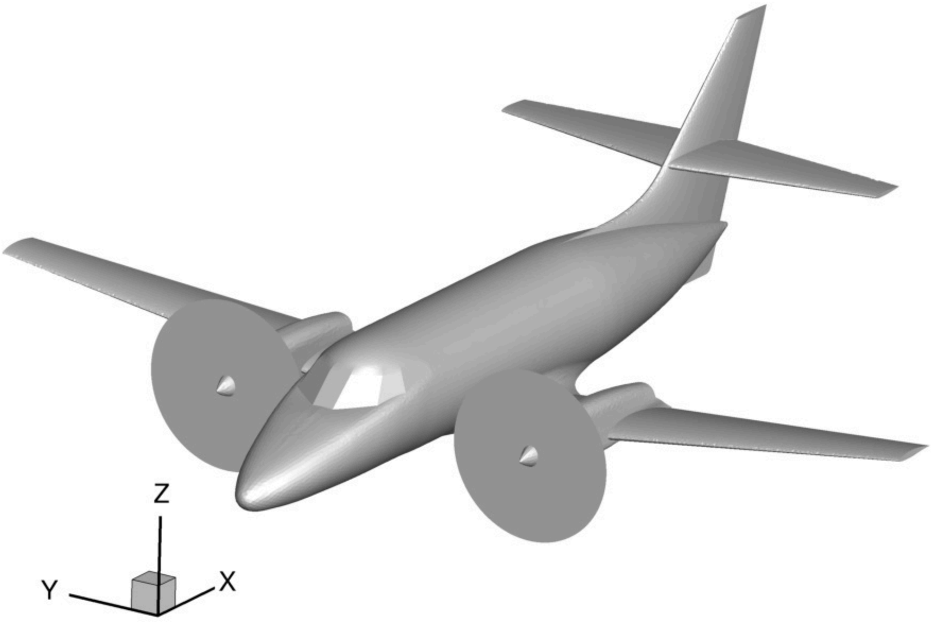

Figure 4: Outer domain of the Jetstream 31 aircraft model for computational purposes

As part of the pressure far field conditions, three-dimensional (3D) flow components have been applied as farfield boundary condition in the outer cylindrical domain, together with Mach number, while the aircraft surfaces are set as a no-slip wall condition. A fixed altitude of 7000ft has been considered as the flight test was completed at this altitude, and so the operating pressure was set to 78060 Pa. The equivalent air speed (EAS) recorded by the aircraft has been transformed in true air speed (TAS) using the relation

$$V_{TAS} = V_{EAS}\sqrt{\frac{\rho}{\rho_0}}, \tag{38}$$

where ρ is the ISA density at 7000ft and ρ_0 the sea-level density. The fuselage pitch angle θ, based on the fuselage centreline, has been taken as pitching angle of the full aircraft and, together with the sideslip angle β, they define the flow direction. Different cases of pitch and sideslip angles have been studied for both right or left engine inoperative. Tables 9 and 10 show all the different configurations.

Case	TAS (m/s)	Mach	θ (deg)	β (deg)	Δt (s)	Total Time (s)
R1	94.597	0.2824	2.9	4.8	0.006076	4.5572
R2	88.896	0.2654	3.7	3.0	0.006466	4.8495
R3	81.854	0.2448	4.8	4.3	0.007022	5.2667
R4	75.484	0.2258	6.3	5.5	0.007615	5.7111
R5	71.029	0.2121	7.3	8.3	0.008093	6.0694
R6	66.409	0.1983	8.7	8.2	0.008655	6.4916
R7 (100%)	90.500	0.2707	3.7	3.8	0.006351	4.7635

Table 9: Right engine off configurations

Case	TAS (m/s)	Mach	θ (deg)	β (deg)	Δt (s)	Total Time (s)
L1	93.032	0.2773	3.3	0.0	0.006179	4.6339
L2	83.060	0.2480	5.2	0.2	0.006920	5.1902
L3	77.183	0.2309	6.4	-1.2	0.007447	5.5854
L4	72.678	0.2170	7.3	-0.3	0.007909	5.9317
L5	68.588	0.2048	9.5	-2.8	0.008380	6.2854
L6 (100%)	91.170	0.2722	3.4	-0.8	0.006305	4.7285

Table 10: Left engine off configurations

During tests, the first 3 recordings of both flight configurations had the feathered propeller rotating slowly at less than 0.5 Hz, while only cases R4 to R7 and L4 to L6 had the inoperative propeller fully stopped. In either case, the drag change with the propeller slow rotating or not were assumed to be negligible. Cases R7 and L6 are at 100% power of the operative engine, all the others at 97%. The turbulence model chosen for RANS simulation is the *standard k-ε*, as verified to be the best one for this case study [42]. Implicit formulation with Roe-FDS flux type and Least Squares Cell Based gradient scheme have been chosen, with a Courant number of 5. After a first longer RANS simulation, 2000 iterations were shown to be enough to reach a converged solution. In order to fasten DES simulations, they have been initialized with RANS results: the *Realizable* k-ε model was then the most obvious choice to model the sub-layer, in order to have coherence between the two solutions. All RANS simulations were running on the Astral supercomputer in Cranfield University with 64 processors, taking approximately 2 hours for each case, while DES simulations with 80 processors were requiring around 6 hours for each case. Despite of the fact that the computational time using the DES approach is three times longer than using the RANS approach, 6 hours compared to 2 hours can be seen as a reasonable computational time nowadays from an engineering point-of-view as well. Furthermore, turbulent flows are inherently unsteady in nature, therefore, one of our goals is to obtain time-dependent simulation results within a reasonable computational time with an improved accuracy. Thus, a further reason to pursue a DES solution, is not just to improve the overall time-averaged comparisons between CFD methods, but to provide the capability to study the unsteady nature of selected areas of the flow.

4. Results and Discussions

In this section, the numerical simulation results are presented and compared with data available in the literature. For simplicity and briefness in the analysis, we will refer to the cases R1, R6, L1 and L5, which are respectively the cases for Right engine off (low and high angle of attack) and Left engine off (low and high angle of attack).

4.1. Convergence properties of the numerical solution

Before analysing results, the actual y^+ value and residuals have been monitored in all RANS and DES simulations. The wall space distance defined in the mesh-strategy was equally found in the solution. In regards to residuals, RANS simulations stabilised around $4 \cdot 10^{-3}$ and $1 \cdot 10^{-2}$ respectively for right-engine-off and left-engine-off cases, DES simulations, which are initialised with RANS solution, maintained these respective values.

4.2. The drag (C_D) and lift (C_L) coefficients

Tables 11 and 12 show drag and lift coefficients of all cases with both RANS and DES against flight test values. The percentage Δ shows that for all cases, the CFD results are within around 10% of the flight test C_L and C_D values. Part of the variation in the comparisons will be due to variations in the flight test data which originate from the test conditions with single engine flight and the limited size of the data set. Further consideration of the DES and RANS data also shows the DES data to have overall improvement of 20% in prediction of the flight test values for the DES data. Clearly additional flight test data would improve these comparisons.

	Flight test		RANS				DES			
Case	C_L	C_D	C_L	$\Delta_{rel}(\%)$	C_D	$\Delta_{rel}(\%)$	C_L	$\Delta_{rel}(\%)$	C_D	$\Delta_{rel}(\%)$
R1	0.5027	0.0423	0.5421	7.8	0.0459	8.6	0.5291	5.2	0.0427	0.9
R2	0.5686	0.0467	0.6112	7.5	0.0479	2.7	0.5998	5.5	0.0445	-4.7
R3	0.6666	0.0568	0.7093	6.4	0.0559	-1.6	0.6966	4.5	0.0521	-8.2
R4	0.7805	0.0674	0.8286	6.2	0.0682	1.2	0.8160	4.6	0.0641	-4.8
R5	0.8817	0.0785	0.8863	0.5	0.0817	4.0	0.8612	-2.3	0.0771	-1.8
R6	1.0054	0.0904	0.9432	-6.2	0.0938	3.8	0.9072	-9.8	0.0886	-2.0
R7	0.5430	0.0442	0.6166	13.6	0.0490	10.7	0.6046	11.3	0.0455	3.0
$\Delta_{avg}(\%)$				6.9		4.7		6.2		3.6

Table 11: C_D and C_L with percentage relative error: Right engine off

	Flight test		RANS				DES			
Case	C_L	C_D	C_L	$\Delta_{rel}(\%)$	C_D	$\Delta_{rel}(\%)$	C_L	$\Delta_{rel}(\%)$	C_D	$\Delta_{rel}(\%)$
L1	0.5285	0.0450	0.5684	7.5	0.0450	0.1	0.5541	4.8	0.0417	-7.3
L2	0.6576	0.0563	0.7311	11.2	0.0566	0.5	0.7190	9.3	0.0529	-6.1
L3	0.7567	0.0642	0.8230	8.8	0.0659	2.6	0.8089	6.9	0.0616	-4.1
L4	0.8531	0.0753	0.8782	2.9	0.0727	-3.5	0.8609	0.9	0.0680	-9.7
L5	0.9508	0.0922	0.9878	3.9	0.0949	3.0	0.9631	1.3	0.0884	-4.1
L6	0.5440	0.0427	0.5789	6.4	0.0459	7.5	0.5641	3.7	0.0422	-1.1
$\Delta_{avg}(\%)$				6.8		2.9		4.5		5.4

Table 12: C_D and C_L with percentage relative error: Left engine off

In order to provide a further validation against flight test data, error bar bands have been defined for a 95% confidence interval. The latter have been obtained with the y-error times the standard deviation (equal to 3 in this case). In Figure 5, all the computed coefficients, flight test data and tendency lines are represented, together with error bars as black vertical lines. Most of the aerodynamic coefficients are found inside the error bands: 70% of the right engine off coefficients and 93% of the left off are within the error bars, giving a global agreement of 80% throughout all the cases.

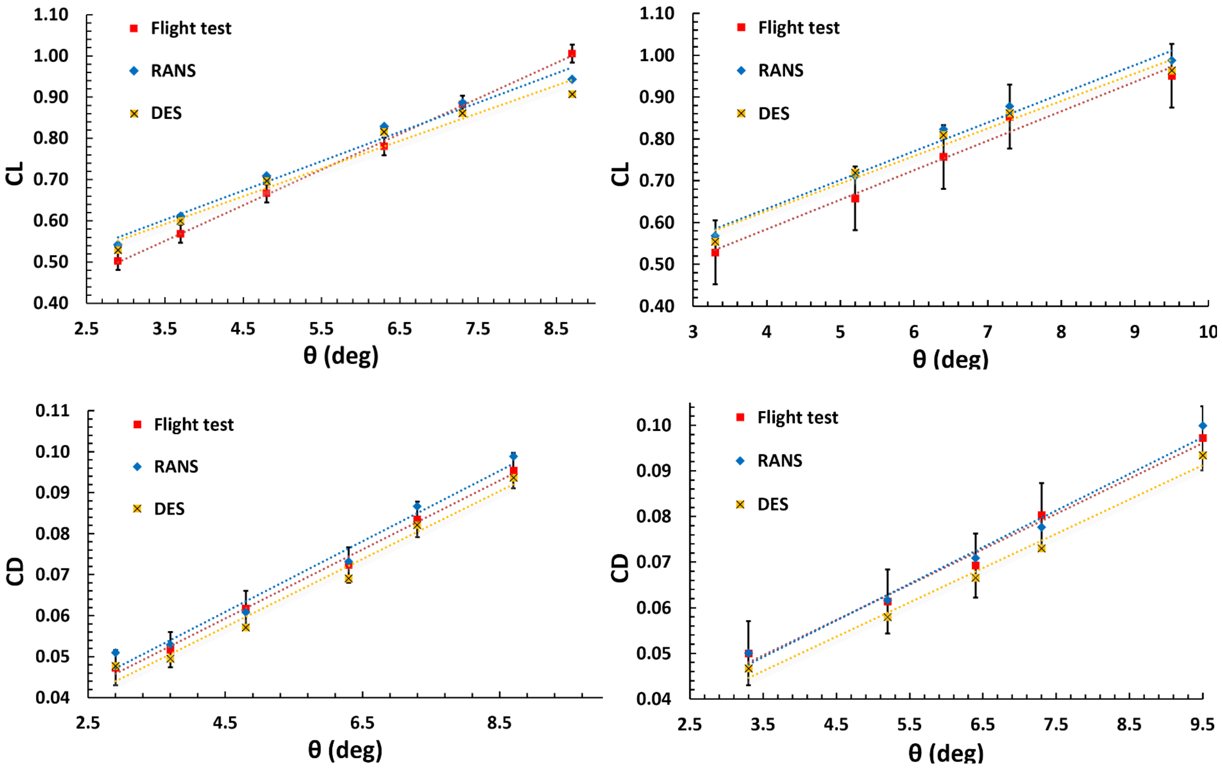

Figure 5: Error bars for a 95% confidence interval - Right engine off on the left side and Left engine off on the right side

4.3. *Moment coefficients and surface deflections*

Aerodynamic moments play a significant role in a one-engine-inoperative condition. In the flight test environment, direct moments cannot be measured in flight and therefore are indirectly estimated from aerodynamic surface deflections, including the elevator, rudder and ailerons. These deflection angles are measured from sensors on the NFLC aircraft when the aircraft is in a trimmed condition, i.e., when the net moments on the aircraft are zero. In general, the changes in moments about the longitudinal (X), lateral (Y) and directional (Z) axes are proportional to the changes in elevator, aileron and rudder angle respectively.

In the CFD model presented in this paper, however, control surfaces were not modelled. However, the CFD model will still allow the calculation of a net moment on the body from any given solution. Therefore, in the following section of the paper, the changes in longitudinal, lateral and directional moments in the CFD model will be normalised and compared to normalised changes in the flight test elevator, aileron and rudder angle.

Moment coefficients have been exported with reference to the aircraft body axes X-Y-Z (see Figure 4). In this way, the moments calculated will represent the aircraft behaviour independently from its orientation in respect to the airflow and the reference system will always be the same. It is reminded that

- a positive elevator angle (η) deflection brings the surface downwards, increasing tail lift;
- a positive rudder angle (ζ) deflection brings the surface to the left, generating an anti-clockwise yaw moment;
- a positive ailerons angle (ξ) deflection is in a way the right wing goes downwards and the left wing upwards.

	Deflections [deg]			RANS			DES		
Case	η	ζ	ξ	C_m	C_n	C_l	C_m	C_n	C_l
R1	-2.2	0.7	10.5	0.008	-0.113	0.126	0.006	-0.113	0.132
R6	-5.3	5.5	20.9	-0.188	-0.151	0.275	-0.189	-0.147	0.298
L1	-2.7	-2.3	-7.9	0.030	-0.008	-0.036	0.029	-0.008	-0.037
L5	-5.6	-5.8	-17.8	-0.160	0.042	-0.199	-0.169	0.040	-0.197

Table 13: Surface deflection and moment coefficients of low and high angles of attack cases

The elevator angle was found negative in all cases. This leads the tail to generate downforce to counter the moment generated between the aircraft aerodynamic centre and the aircraft centre of gravity (CoG). From the CFD simulations, pitching coefficients C_m are mostly negative values, demonstrating the necessity of an elevator deflection, although it should be noted, the CFD model does not account for the moments about the longitudinal axes, associated with the CoG of the aircraft.

In the right engine off configurations, positive deflections of both rudder and ailerons have been adopted in flight test. The positive rudder deflection counters the asymmetric thrust from the left engine, generating a sideslip force on the right. This creates a lateral component of flow resulting in a greater lift distribution on the right wing, from which the necessity of a positive aileron deflection to counter the rolling moment. This is effectively rolling moment due to sideslip, a result of the lateral stability of the aircraft. In the CFD model, negative yaw coefficients C_n reveals the aerodynamics moment globally generated by the aircraft goes in support of the asymmetric thrust moment, not reproduced in the simulation. In this case, the sideslip angle acts as an angle of attack for the rudder airfoil, generating a lateral "lift" force increasing the yaw moment. Roll coefficients C_l are in this case all positive, which means the right wing lifts and the left wing would drop. Similar considerations can be drawn for left engine off cases, where the yaw and roll coefficients have opposite sign values.

In order to determine whether the trend between surface deflection angles in flight test and moment coefficients in CFD was realistic, a normalized comparison has been carried out for R1 to R6 and L1 to L5 cases. An overall close agreement has been achieved through this analysis, as shown by plots in Figure 6. The average percentage deviation has been calculated for each curve and reported in Table 14, where deviations of 3.3% to 7.0% can be found.

Case	RANS			DES		
	Pitch - C_m	Yaw - C_n	Roll - C_l	Pitch - C_m	Yaw - C_n	Roll - C_l
Right off	3.91%	6.20%	5.13%	3.74%	6.46%	5.91%
Left off	7.01%	4.47%	3.48%	6.15%	4.83%	3.29%

Table 14: Percentage average deviation of surface deflections and moment coefficients

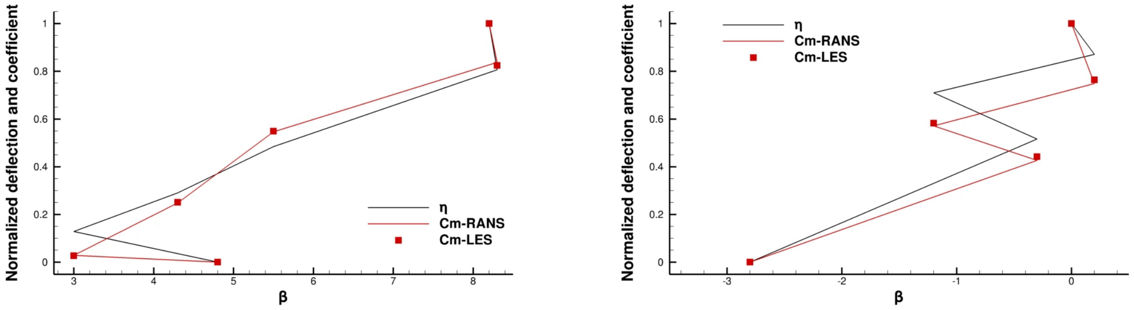

(a) Elevator deflection and C_m over sideslip angle β

(b) Elevator deflection and C_m over sideslip angle β

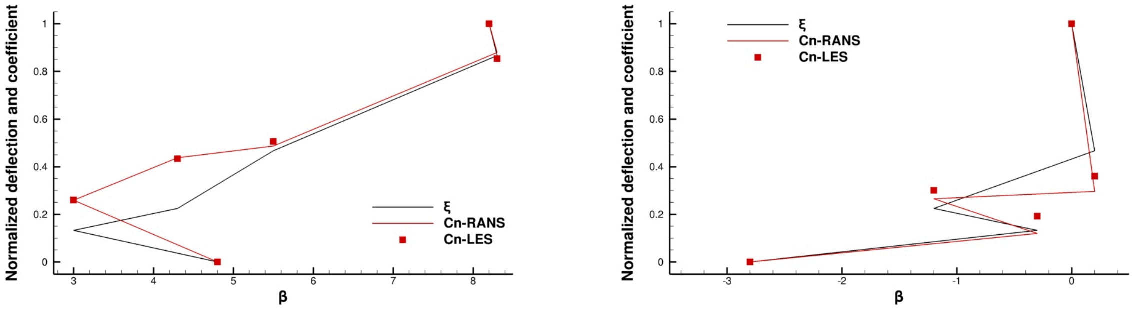

(c) Rudder deflection and C_n over sideslip angle β

(d) Rudder deflection and C_n over sideslip angle β

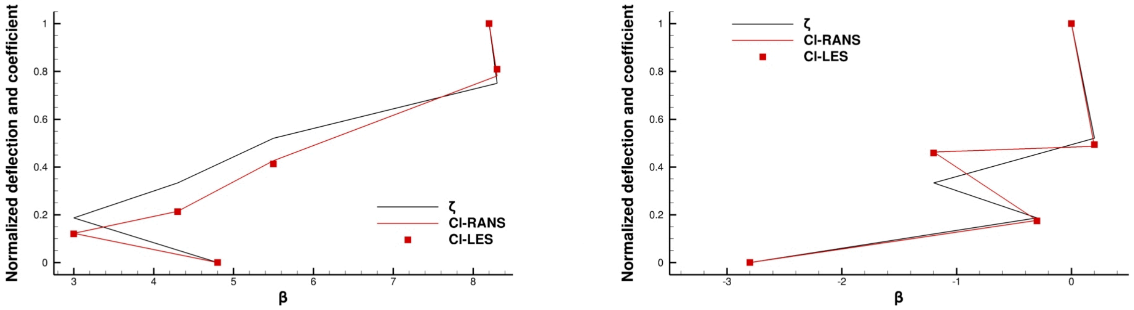

(e) Aileron deflection and C_l over sideslip angle β

(f) Aileron deflection and C_l over sideslip angle β

Figure 6: Comparison between normalized deflection angles and moment coefficients where (a), (c), (e): Right engine off and (b), (d), (f): Left engine Off cases

4.4. Pressure coefficients

Another important aspect to consider in aircraft aerodynamics analyses is the pressure coefficient distribution. The dimensionless pressure coefficient is defined by

$$C_p = \frac{p - p_\infty}{\frac{1}{2}\rho_\infty V_\infty^2}, \tag{39}$$

where the ∞ subscript indicates the free-stream condition. A spanwise line has been defined at X = 6 *m* and a supplementary 3D view of the top surface is also given. This line allows analysis of the effect of the single engine conditions on the wing loading. First, a comparison between right engine off and left engine off cases is done at low angle of attack (at coordinate X = 6 *m*) and it is shown in Figure 7. The pressure coefficient follows a very similar trend between the two cases except in the proximity of the nacelles. In fact, the user-defined pressure jump condition on the actuator disk gives an asymmetric pressure distribution on the wings. The inoperative engine wing, which is under sideslip, is thus subject to a higher (in module) pressure load in the engine nacelle region.

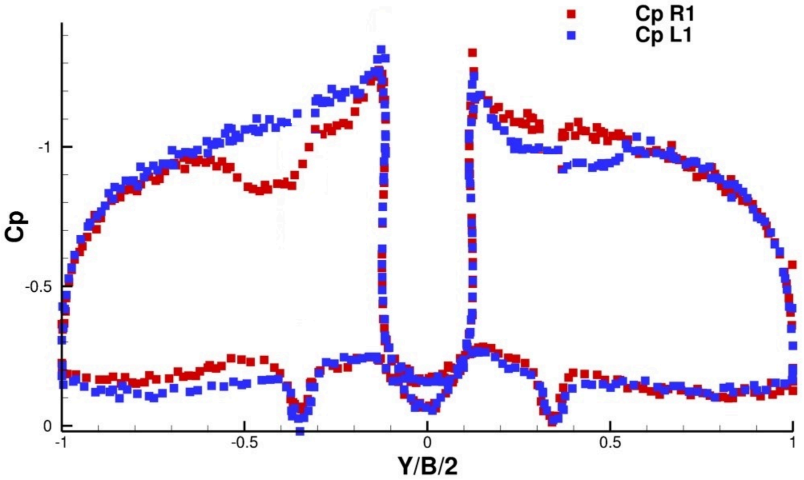

Figure 7: Spanwise pressure coefficient at low angle of attack: comparison right and left engine off cases

Figure 8 shows a comparison is done between low and high angles of attack for a left engine off case. A higher angle of attack gives a wider pressure gradient between bottom and top aerofoil surfaces, corresponding to a higher lift. In particular, the wing bottom surfaces recorded a pressure coefficient increase of approximately $\Delta(C_p) = 0.2$ points from low to high angle of attack, while the inoperative engine wing showed decrease of up to $\Delta(C_p) = 0.4$. Furthermore, the operative engine wing revealed a C_p decrease of $\Delta(C_p) = 0.2 - 0.4$ from the nacelle to the tip, while the region between nacelle and wing root presents an almost unchanged pressure. This is a further demonstration of the rolling moment generated by the sideslip angle at the high angle of attack with the pressure coefficient distribution of the highly asymmetric case in favour of the inoperative engine wing.

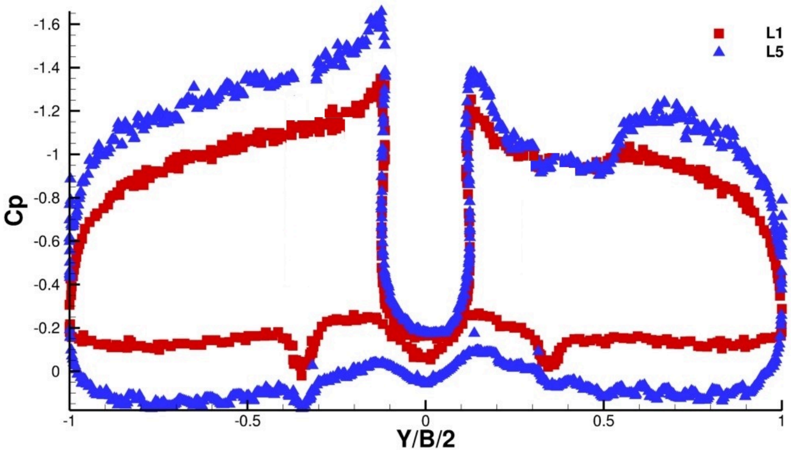

(a) Left engine off

Figure 8: Spanwise pressure coefficient at low and high angles of attack

4.5. *Wake profiles*

The wake profile behind both wings provides information on local spanwise drag coefficients, thus allowing more detailed analysis of the effect of the propeller on the wing. The propeller-wing interaction has been taken into account by using the DES approach. In the following analysis, the high angle of attack R6 case has been taken into consideration. For viscous fluid flows, a zero lift section (2D) drag coefficient (or *drag rake*) can be calculated from locations at different freestream locations [56]. This drag rake evaluation is not valid for separated and stalled flows, further than neglecting the vortex induced drag [57]. For this reason, the low angle of attack case R1 is considered in next analyses. The drag rake per metre c_{d0} can be computed on a line as

$$c_{d0} = 2\int_{y1}^{y2} \left(\sqrt{\frac{q}{q_\infty}} - \frac{q}{q_\infty} \right) \frac{dy}{c} \tag{40}$$

where q is the local dynamic pressure, q_∞ the freestream dynamic pressure and dy the drag rake element spacing. Note that the drag of inoperative propeller was neglected in our model which can be seen as a reasonable assumption, as in reality, the propeller is ’feathered’, a condition where the stationary blades are rotated in alignment with the freestream to minimise drag. Therefore as a first approximation, the drag of the inoperative, feathered propeller will be insignificant, when compared to the overall drag of the rest of the aircraft and lifting surfaces, and therefore can be neglected. A series of parallel lines has been defined as in Table 15 and in Figure 9 in order to estimate the drag rake evolution in the wake region. To define the lines span limits in the wake region, the dynamic pressure on the centreline of these sections was plotted to find the location where the conditions were similar to the freestream, which resulted to be at X = 60 *m* (or 11 chords after the wing trailing edge).

X from TE (X / $\bar{c}$)	Y (*m*)	Z (*m*)
0 to 11	± 3.5	[-2, 2] and [-4, 4]

Table 15: Coordinates of line series

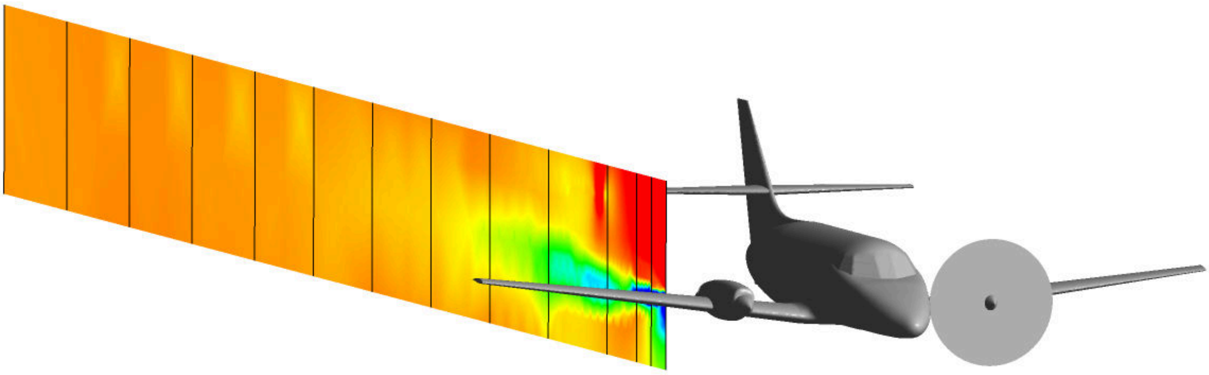

Figure 9: Lines location for wake study over a dynamic pressure contour

In all these sections and behind both wings, the drag rake coefficient has been calculated with two different rake lengths (Z), 4 and 8 meters, and plotted in Figure 10. The inoperative-engine wing, as above showed, has a well defined wake profile disturbed only by the wing surface. The freestream conditions are reached sooner and this results in a drag rake coefficient reaching sooner an asymptotic value ($\approx$ 0.04). The consideration of a wider rake line did not yield a higher drag, as the flow in this region is almost undisturbed. When the propelled wing is considered, sensitive differences can be highlighted. First of all, the drag coefficients are higher in all sections, with a maximum value 6 times bigger than in the opposite wing (0.3 against 0.05). The unsteadiness of this region did not allow values to reach an asymptotic value even after 11 chords behind the trailing edge. However, the trend followed is towards the freestream drag rake value found in the other wing. The fidelity of modelling propeller-wing interaction in the present case depends on the temporal resolution of the DES approach and any future insight will depend on the quality of the unsteady in-flight data that can be recorded from the aircraft. Therefore, in this respect, the use of the DES approach here is ahead of the in-flight measurements. Furthermore, when a wider rake line is considered, a drag rake $\approx$ 0.05 points greater is found, specially in the further domain, explaining how the propeller influenced the flow even in regions wider than the disk diameter. Further corrections to the drag calculation methods are likely to be required to establish a more accurate measure of the drag coefficients in the slipstream regions.

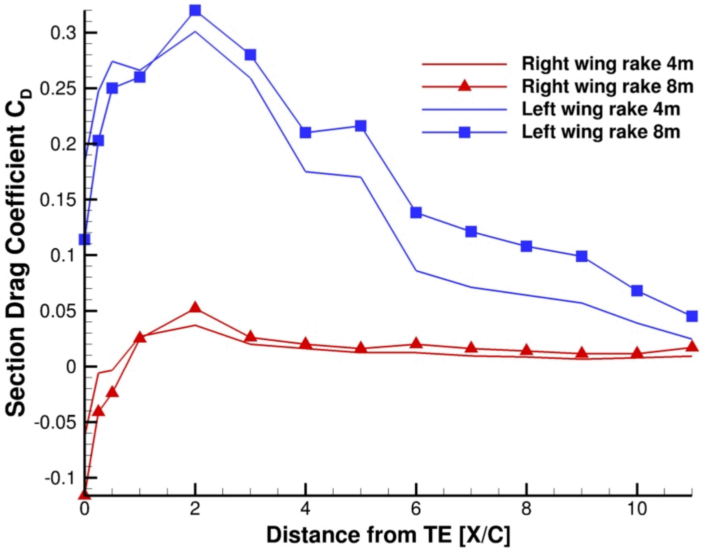

Figure 10: Line location for wake study

Qualitative results on the flow physics of this solution are presented. A common method for vortex visualization is the Q-Criterion, which in this case has been computed by

$$Q = 2\omega_{xy}^2 + 2\omega_{xz}^2 + 2\omega_{yz}^2 - S_{xx}^2 - S_{yy}^2 - S_{zz}^2 - 2S_{xy}^2 - 2S_{xz}^2 - 2S_{yz}^2, \tag{41}$$

where

$$\begin{cases} \omega_{xy} = 0.5\left(\dfrac{\partial u}{\partial y} - \dfrac{\partial v}{\partial x}\right), \\ S_{xy} = 0.5\left(\dfrac{\partial u}{\partial y} + \dfrac{\partial v}{\partial x}\right). \end{cases} \tag{42}$$

Two different values of Q-criterion have been used to define iso-surfaces on the low and high angle of attack cases (see Figure 11). With the first value of Q-criterion (see Figures 11a and 11b), the smaller vortex structures can be seen. Trailing vortexes detaching from the wing tips and vertical fin are captured in both cases. The higher angle of attack case presents trailing vortexes also in the elevator. The most interesting aspect is the separation behind wing trailing edges: as expected, a greater level of turbulence generated and captured in the high angle case, where the transition to a turbulent boundary layer occurs earlier determining a stronger separation from the surface.

Wing areas near the operative engine nacelle also presents an already detached flow. In the second set of Figures (11c and 11d), larger vortexes are visualized. Longer trailing vortexes have been captured in both cases, but the most dominant flow feature is the turbulence derived from the user-defined propeller model, specially in the high attack angle case. A cylindrical surface of vorticity starting from the propeller is indeed visible, which is then dissipating in smaller structures while flowing further in the domain.

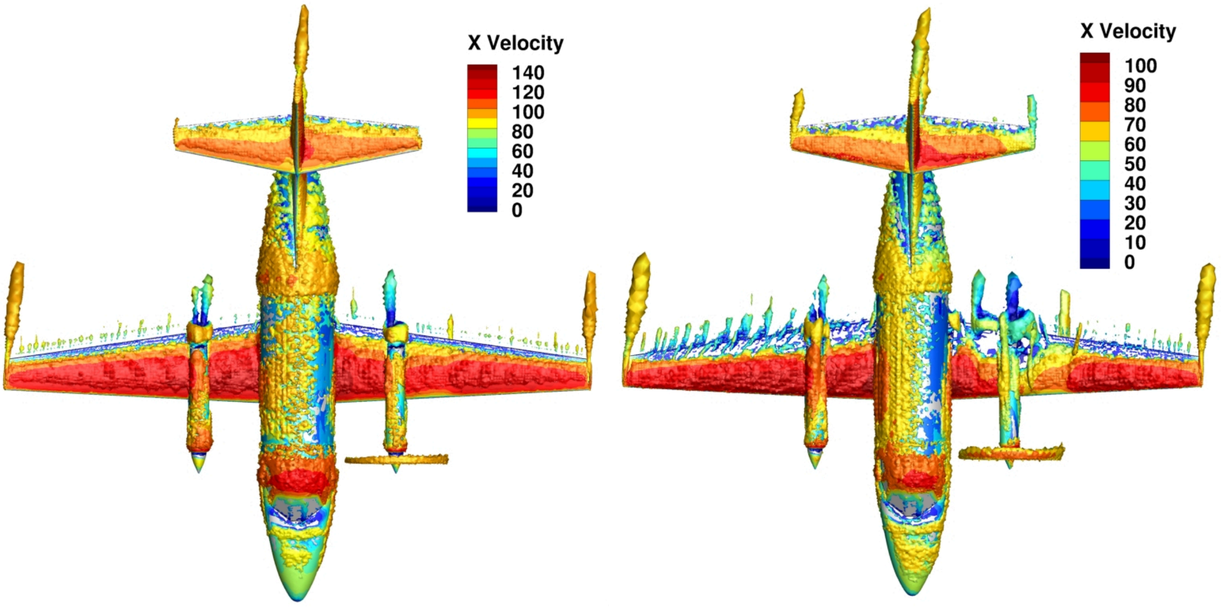

(a) Q=100 - R1 case (b) Q=100 - R6 case

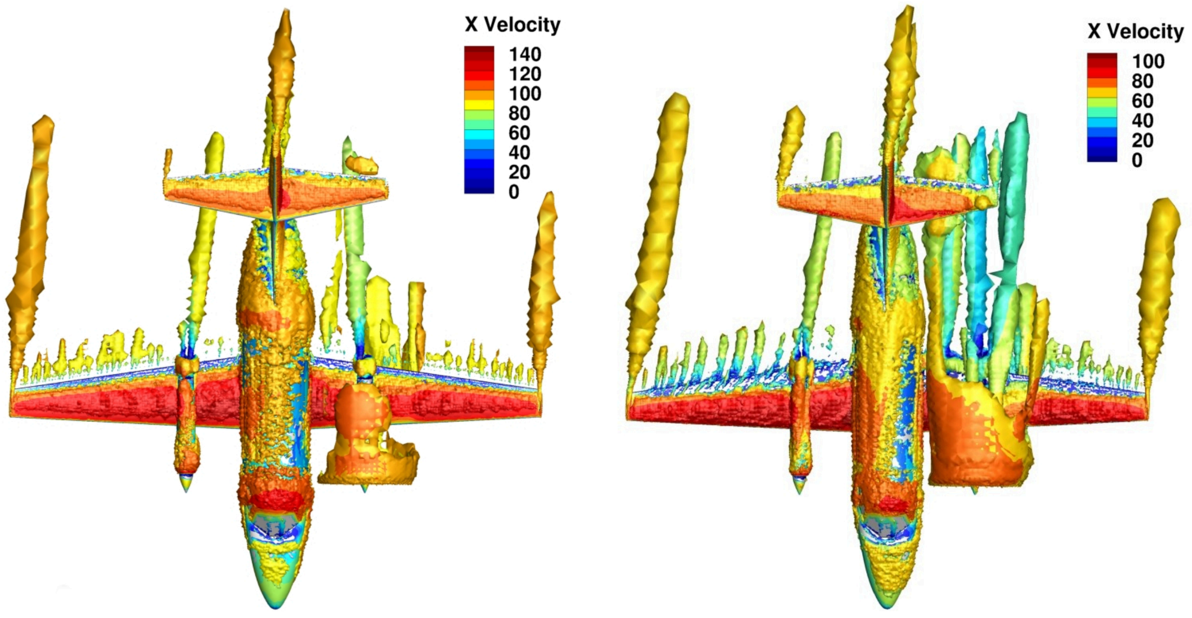

(c) Q=1000 - R1 case (d) Q=1000 - R6 case

Figure 11: Q-Criterion iso-surfaces, coloured by X-Velocity contour

5. Conclusions

In this paper, the most recent advances in a CFD simulation of the Jetstream 31 aircraft of the National Flying Laboratory Centre have been presented. Aerodynamic characteristics are generated of this aircraft in conditions of one engine inoperative using unsteady CFD simulations and to compare with flight test data. Drag and lift coefficients were the main form of validation: percentage deviation are found in a range between 0.1% and 13.6%, with an average deviation around 6.5% for C_L and 4% for C_D in RANS simulations and 5.5% and 4% for DES simulations. Furthermore, drag prediction showed was not strongly influenced by the steady or unsteady turbulence model, while lift coefficient had an improvement of 1% point when solved with and when compared to previous steady models.

From the solutions presented, forces and moments could not be reliably predicted in the CFD, due to the omission of control surface positions and the simplified thrust model for the operative propeller. Regardless this of limitation, the moment coefficients calculated showed a realistic trend when compared to flight data for all cases. To this end, a normalized depiction of control surface deflections in flight test and moment coefficients in CFD simulation revealed an outstanding agreement: the trend has only slight differences in few configurations, with average percentage deviations between 3% and 7%.

Wake profile plots revealed the propeller influence on the wings wake and the sensitive differences between RANS and DES turbulence models for wake prediction. A drag rake has been used to calculate the drag coefficients for different sections in the wake and it confirmed the higher drag due to the turbulent structure behind the operative engine, with a peak of value 0.3 against the 0.05 of the wing with failed engine. Additionally, it has been showed the rake size dependency when the flow is highly turbulent, finding a higher drag with a wider rake for the wake behind the propeller. Contrarily, no significant differences have been found for the failed-engine wing with wider rake.

Overall the work presents the first successfully application of unsteady CFD on a Jetstream 31 aircraft. Further work is required to improve the propeller model and to implement control surface positions, to allow more direct comparisons of the forces and moments of the model with the flight test data. This is the subject of a future paper.

Conflict of Interest

None Declared.

Acknowledgements

The present research work was financially supported by the Centre for Computational Engineering Sciences (CCES) at Cranfield University under project code EEB6001R. The flight tests were successfully performed in the

National Flying Laboratory Centre (NFLC) on the Jetstream 31 aircraft. The authors would like to acknowledge the IT support and the use of the High Performance Computing (HPC) facilities at Cranfield University, UK.

References

[1] J. Blazek, Computational Fluid Dynamics: Principles and Applications, Elsevier, Amsterdam, London, 2001.

[2] J. D. Anderson, Computational Fluid Dynamics: The Basics with Applications, McGraw-Hill, Inc., New York, 1995.

[3] F. T. Johnson, E. N. Tinoco, N. J. Yu, Thirty years of development and application of CFD at Boeing Commercial Airplanes, Computers and Fluids 34 (2005) 1115–1151.

[4] J. A. Ekaterinaris, Prediction of active flow control performance on airfoils and wings, Aerospace Science and Technology 8 (2004) 401–410.

[5] A. Kyrkos, J. A. Ekaterinaris, Assessment of an unstructured mesh approach for CFD predictions of the NH90 fuselage rotor, Aerospace Science and Technology 19 (2012) 77–85.

[6] S. G. Kontogiannis, J. A. Ekaterinaris, Design, performance evaluation and optimization of a UAV, Aerospace Science and Technology 29 (2013) 339–350.

[7] F. Gómez, R. Gómez, V. Theofilis, On three-dimensional global linear instability analysis of flows with standard aerodynamics codes, Aerospace Science and Technology 32 (2014) 223–234.

[8] M. Ghoreyshi, K. Ryszka, R. M. Cummings, A. J. Lofthouse, Vortical flow prediction of a diamond wing with rounded leading edges, Aerospace Science and Technology 57 (2016) 103–117. Diamond Wing Aerodynamics.

[9] S. Kontogiannis, D. Mazarakos, V. Kostopoulos, ATLAS IV wing aerodynamic design: From Conceptual approach to detailed optimization, Aerospace Science and Technology 56 (2016).

[10] D. M. Nelson, J. P. Irving, M. Ghoreyshi, A. Jirasek, A. J. Lofthouse, Experimental and numerical investigation of flight dynamics of a generic lambda wing configuration, Aerospace Science and Technology 71 (2017) 706–724.

[11] N. J. Lawson, H. Jacques, J. E. Gautrey, A. K. Cooke, J. C. Holt, K. P. Garry, Jetstream 31 National Flying Laboratory: Lift and Drag Measurement and Modelling, Aerospace Science and Technology 60 (2017) 84–95.

[12] T. Misaka, S. Obayashi, Numerical study on jet-wake vortex interaction of aircraft configuration, Aerospace Science and Technology 70 (2017) 615–625.

[13] M. Righi, V. Pachidis, L. Könözsy, L. Pawsey, Three-dimensional through-flow modelling of axial flow compressor rotating stall and surge, Aerospace Science and Technology 78 (2018) 271–279.

[14] U. Piomelli, Large-Eddy and Direct Simulation of Turbulent Flow, 9e conference annuelle de la Societe canadienne de CFD (2001).

[15] M. Gharib, Perspective: the experimentalist and the problem of turbulence in the age of supercomputers, Trans. ASME, J. Fluids Eng. 118 (1996) 233–242.

[16] J. Smagorinsky, General Circulation Experiments with the Primitive Equations, Mon. Weath. Rev. 93 (1963) 99–165.

[17] D. R. Chapman, Computational aerodynamics development and outlook, AIAA journal 17 (1979) 1293–1313.

[18] P. R. Spalart, W.-H. Jou, M. Strelets, S. R. Allmaras, Comments on the feasibility of LES for wings, and on a hybrid RANS/LES approach, 1st AFOSR Int. Conf. on DNS/LES (1997).

[19] P. R. Spalart, W.-H. Jou, M. Strelets, S. R. Allmaras, Comments on the feasibility of LES fow wings, and on a hybrid RANS/LES approach, Advances in DNS/LES 1 (1997) 4–8.

[20] M. L. Shur, P. R. Spalart, M. Strelets, M. Travin, Detached Eddy Simulation of an Airfoil at High Angle of Attack, Engineering Turbulence Modelling and Experiments 4 (1999) 669–678.

[21] P. R. Spalart, Detached-Eddy Simulation, Annual Review of Fluid Mechanics 41 (2009) 181–202.

[22] L. Jacquin, D. Fabre, D. Sipp, V. Theofilis, H. Vollmers, Instability and unsteadiness of aircraft wake vortices, Aerospace Science and Technology 7 (2003) 577–593.

[23] H. Huang, K. Ekici, An efficient harmonic balance method for unsteady flows in cascades, Aerospace Science and Technology 29 (2013) 144–154.

[24] M. Ghoreyshi, A. Jirásek, R. M. Cummings, Computational approximation of nonlinear unsteady aerodynamics using an aerodynamic model hierarchy, Aerospace Science and Technology 28 (2013) 133–144.

[25] M. Ghoreyshi, R. M. Cummings, Unsteady aerodynamics modeling for aircraft maneuvers: A new approach using time-dependent surrogate modeling, Aerospace Science and Technology 39 (2014) 222–242.

[26] U. Bunge, C. Mockett, F. Thiele, Guidelines for implementing Detached-Eddy Simulation using different models, Aerospace Science and Technology 11 (2007) 376–385.

[27] S. Lawson, G. Barakos, Evaluation of DES for weapons bays in UCAVs, Aerospace Science and Technology 14 (2010) 397–414.

[28] D. Sun, Q. Li, H. Zhang, Detached-eddy simulations on massively separated flows over a 76/40° double-delta wing, Aerospace Science and Technology 30 (2013) 33–45.

[29] R. M. Cummings, A. Schütte, Detached-Eddy Simulation of the vortical flow field about the VFE-2 delta wing, Aerospace Science and Technology 24 (2013) 66–76. VFE-2.

[30] M. Mirzaei, A. Sohankar, The evaluation of a detached eddy simulation based on the $k-\omega-\overline{\upsilon^2}-f$ model with three flow configurations, Aerospace Science and Technology 43 (2015) 199–212.

[31] B. Šekutkovski, I. Kostić, A. Simonović, P. Cardiff, V. Jazarević, Three-dimensional fluid-structure interaction simulation with a hybrid RANS-LES turbulence model for applications in transonic flow domain, Aerospace Science and Technology 49 (2016) 1–16.

[32] F. Nicolás-Pérez, F. Velasco, J. García-Cascales, R. Otón-Martínez, A. López-Belchí, D. Moratilla, F. Rey, A. Laso, On the accuracy of RANS, DES and LES turbulence models for predicting drag reduction with Base Bleed technology, Aerospace Science and Technology 67 (2017) 126–140.

[33] L. Zhou, R. Zhao, W. Yuan, An investigation of interface conditions inherent in detached-eddy simulation methods, Aerospace Science and Technology 74 (2018) 46–55.

[34] L. Casadei, CFD Study of Jetstream 31 Aerodynamics Performance with One Engine Inoperative, Master's thesis, Cranfield University, 2017.

[35] X. Wang, L. Cai, Mathematical modeling and control of a tilt-rotor aircraft, Aerospace Science and Technology 47 (2015) 473–492.

[36] Y. Choi, H. Jimenez, D. N. Mavris, Statistical gain-scheduling method for aircraft flight simulation, Aerospace Science and Technology 46 (2015) 493–505.

[37] K. Yue, L. Cheng, T. Zhang, J. Ji, D. Yu, Numerical simulation of the aerodynamic influence of an aircraft on the hose-refueling system during aerial refueling operations, Aerospace Science and Technology 49 (2016) 34–40.

[38] T. Xiao, N. Qin, Z. Lu, X. Sun, M. Tong, Z. Wang, Development of a smoothed particle hydrodynamics method and its application to aircraft ditching simulations, Aerospace Science and Technology 66 (2017) 28–43.

[39] Z. Li, L. Zhang, H. Liu, Z. Zuo, C. Liu, Nonlinear robust control of tail-sitter aircrafts in flight mode transitions, Aerospace Science and Technology 81 (2018) 348–361.

[40] Z. Wu, B. Lv, Y. Cao, Heavy rain effects on aircraft lateral/directional stability and control determined from numerical simulation data, Aerospace Science and Technology 80 (2018) 472–481.

[41] H. K. Versteeg, W. Malalasekera, An introduction to Computational Fluid Dynamics, The Finite Volume Method, second edition ed., Pearson Education Limited, Prentice Hall, Harlow, England, 2007.

[42] H. Jacques, Simulation of propeller effects on the Jetstream 31 aircraft, Master's thesis, Cranfield University, 2014.

[43] M. Germano, U. Piomelli, P. Moin, W. H. Cabot, Dynamic Subgrid-Scale Eddy Viscosity Model, In Summer Workshop (1997).

[44] D. K. Lilly, A Proposed Modification of the Germano Subgrid-Scale Closure Model, Physics of Fluids 4 (1992) 633–635.

[45] M. Le Pajolec, Investigation of Propeller theories on BAE Jetstream 31 CFD Model, Master's thesis, Cranfield University, 2013.

[46] R. D. Archer, M. Saarlas, An Introduction to Aerospace Propulsion, Prentice-Hall, Inc., London, United Kingdom, 1996.

[47] W. S. Westmoreland, R. W. Tramel, J. Barber, Modelling propeller flow fields using CFD, AIAA Paper (2008).

[48] W. F. Phillips, Mechanics of Flight, John Wiley & Sons, Inc., New York, 2010.

[49] G. J. D. Zondervan, A Review of Propeller Modelling Techniques Based on Euler Methods, Technical Report, Delft University Press, The Netherlands, 1995.

[50] M. Lino, Numerical Investigation of Propeller-Wing Interaction Effects for a Large Military Transport Aircraft, Master's thesis, Delft University of Technology, The Netherlands, 2010.

[51] C. A., Data pack for the jetstream 31, Flight Dynamics Principles assignment, unpublished, Cranfield University (2013).

[52] J. T. Hwang, J. R. Martins, An unstructured quadrilateral mesh generation algorithm for aircraft structures, Aerospace Science and Technology 59 (2016) 172 – 182.

[53] R. Djeddi, K. Ekici, Solution-based adaptive mesh redistribution applied to harmonic balance solvers, Aerospace Science and Technology 84 (2019) 543–564.

[54] P. J. Roache, Verification and Validation in Computational Science and Engineering, Hermosa Publishers: Albuquerque, New Mexico, USA, 1998.

[55] D. J. Mavriplis, Grid Quality and Resolution Issues from the Drag Prediction Workshop Series, Journal of Aircraft 46 (2009) 935–950.

[56] N. Lawson, ANSYS Fluent User Guide - 3D CFD Solutions, National Flying Laboratory Centre, Cranfield University, 2017.

[57] J. Williams, J. Barlow, R. Ranzenbach, Experimental Study of CD Variation With Aspect Ratio, SAE Technical Paper Series (1999).

Nomenclature

Abbreviations

CFD	Computational Fluid Dynamics
CoG	Centre of Gravity
DES	Detached-Eddy Simulation
DDES	Delayed Detached-Eddy Simulation
DNS	Direct Numerical Simulation
DSLM	Dynamic Smagorinsky-Lilly Model
EAS	Equivalent Air Speed
GCI	Grid Convergence Index
GMT	General Momentum Theory
ISA	International Standard Atmosphere
LES	Large-Eddy Simulation
NFLC	National Flying Laboratory Centre
OEI	One Engine Inoperative
RANS	Reynolds-Averaged Navier-Stokes
SGS	Subgrid-Scale
TAS	True Air Speed
UDF	User-Defined Function
URANS	Unsteady RANS
ZFM	Zero-Fuel Mass

Symbols

A_1, B_1, C_1	Parameters (-)
AT	Air Temperature (K)
C	Filtering Independent Constant (-)
C_D	Drag Coefficient (-)
C_{des}	Constant of the DES Approach (-)
C_L	Lift Coefficient (-)
C_l, C_m, C_n	Moment Coefficients (-)
C_s	Smagorinsky Constant (-)
d	Distance to the Closest Wall (m)
D	Drag Force (N)
D_k	Dissipation Term (Kg/ms)
f_d	Distance Function (m)
H	Altitude (m)
k	Turbulent Kinetic Energy (m^2/s^2)
l	Characteristic Length (m)
L	Lift Force (N)
L_{ij}	Resolved Turbulent Stresses (Kg/ms^2)
L_s	Subgrid-Scale Mixing Length (m)
M_{ij}	Anisotropic Part of the T_{ij} Tensor (Kg/ms^2)
p_∞	Ambient Pressure (Pa)
r_p	Propeller Radius (m)
R	Universal Gas Constant ($J/molK$)
Re	Reynolds Number (-)
S_{ij}	Mean Rate-of-Strain Tensor ($1/s$)
t_{conv}	Convective Time (s)
T	Thrust (N)
T_{ij}	Filtered Subgrid-Scale Stresses (Kg/ms^2)
T_∞	Reference Temperature (K)
u_i'	Fluctuating Velocity Vector (m/s)
V_i	Induced Velocity (m/s)
V_t	Tangential Velocity (m/s)
V_∞	Free Stream Velocity (m/s)
W	Aircraft Weight (Kg)
W_f	Fuel Mass (Kg)
$-\rho\overline{u_i'u_j'}$	Reynolds Stress Tensor (Kg/ms^2)

Greek Symbols

α	Wing Angle of Attack (degree)
β	Sideslip Angle (degree)
γ	Grid Refinement Ratio (-)
δ_{ij}	Kronecker delta or Unit Tensor (-)
$\delta(x)$	Boundary Layer Thickness (m)
ε	Rate of Dissipation (m^2/s^3)
ζ	Positive Rudder Angle (degree)
η	Positive Elevator Angle (degree)
θ	Pitch Angle (degree)
κ	von Kármán Constant (-)
μ_t	Dynamic Eddy Viscosity (Pas)
ν	Kinematic Viscosity (m^2/s)
ν_t	Kinematic Eddy Viscosity (m^2/s)
ξ	Positive Ailerons Angle (degree)
ρ	Fluid Density (Kg/m^3)
$\overline{\rho}$	Filtered Density (Kg/m^3)
ρ_∞	Reference Density (Kg/m^3)
τ_{ij}	Subgrid-Scale Stresses (Kg/ms^2)
Δ	Local Grid Size (m)
$\hat{\Delta}$	Twice of the Local Grid Scale (m)
Δ_{avg}	Average Relative Error (%)
Δ_{max}	Maximum Grid Spacing (m)
Δ_{rel}	Relative Error (%)
Δt	Time Step (s)
Ω	Propeller Rotational Speed (rad/s)

2019-05-15

Unsteady Detached-Eddy Simulation (DES) of the Jetstream 31 aircraft in One Engine Inoperative (OEI) condition with propeller modelling

Casadei, Loris

Elksevier

Casadei L, Könözsy L, Lawson NJ. (2019) Unsteady Detached-Eddy Simulation (DES) of the Jetstream 31 aircraft in One Engine Inoperative (OEI) condition with propeller modelling. Aerospace Science and Technology, Volume 91, August 2019, pp. 287-300

https://doi.org/10.1016/j.ast.2019.05.034